PAPER • OPEN ACCESS

Stress and deformation of ceramic rolls to produce high quality zinc coated steel sheet

View the article online for updates and enhancements.

Stress and deformation of ceramic rolls to produce high quality zinc coated steel sheet

Hiromasa SAKAI[1], Nao-Aki NODA[1], Yoshikazu SANO[1], Yasushi TAKASE[1] and Guowei ZHANG [1]

[1]Department of Mechanical and Control Engineering, Kyushu Institute of Technology Sensui-Cho 1-1 Tobata-Ku, Kitakyushu-Shi, Fukuoka, Japan

E-mail: q595103h@mail.kyutech.jp

Abstract. Several ceramic rolls can be used efficiently to produce high quality zinc coated steel sheet used for automobiles. Those ceramics rolls may provide a longer life and reduce the cost for the maintenance because of its large heat resistance and large wear resistance. One example may be seen in sink rolls used in molten zinc bath to manufacture zinc coated steel sheet. Since the rolls are subjected to large thermal stress and mechanical loading, care should be taken for the risk of fracture due to the ceramic brittleness. Moreover, since the sleeve and shafts can be connected only by using small shrink fitting ratio， another failure risk should be considered for the separation of those components [25, 26]. In this paper, therefore, the mechanical and thermal stress and separation condition will be investigated considering the separation of the connected portion. Here, by using the finite volume method the heat transfer coefficient is discussed and by using the finite element method the thermal stress is considered.

1. Introduction

In steelworks, steel manufacturing machinery produces heavy plates, hot-rolled strips, cold-rolled strips, which are used in a broad range of the fields, such as automobiles, electrical appliances, and steel frames for construction. Steel manufacturing machinery includes several types of rolls and rollers, which are used in severely corrosive atmosphere. The first example is found in sink and support rolls used in molten zinc bath to manufacture zinc coated steel sheet. The second example may be seen in conveying rollers used in hot rolling line to transport hot strip. Since those rolls and rollers are used under high temperature and corrosive atmosphere, abrasion and corrosion easily arise on their surfaces in a short period. Therefore, instead of stainless steel rolls and rollers, ceramic rolls and rollers are recently considered to be used [1-8]. Since the ceramics has high heat resistance and abrasion resistance [9], the exchanging cycle of roll and roller can be extended in a large scale. In this paper, we will also focus on the two examples of rolls, first in continuous pickling line [10, 11], second in molten zinc bath [12]. Then, the application of ceramic rolls will be considered in the following sections.

2. Static Strength Analysis and Fatigue Strength Analysis
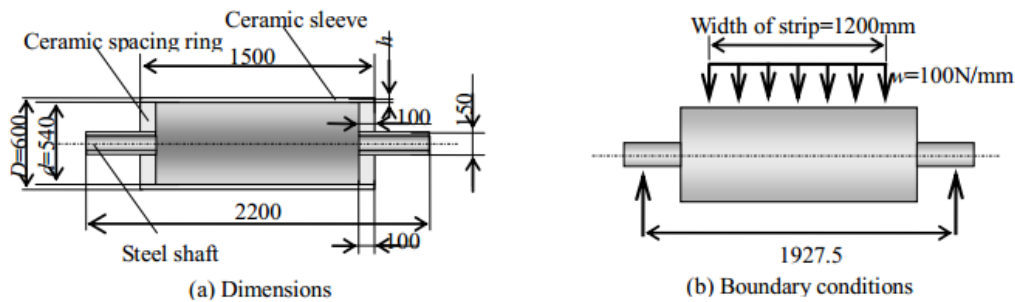
2.1. Analytical Conditions
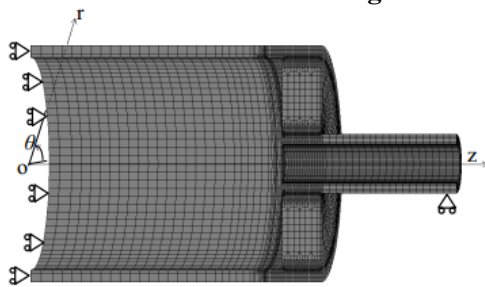
Figure 1 Ceramics roll dimensions

Figure 2 FEM mesh

Table 1 Material properties

	Ceramics (Si₃N₄)	Steel (Hv220)
Young's moduls (MPa)	300	210
Poisson's ratio	0.28	0.3
Tensile strength (MPa)	500	600
Fracture toughness (MPa$\sqrt{\text{m}}$)	7	100
Fatigue strength (MPa)	200	300

Define the shrink fitting ratio as δ/d, where δ is the diameter difference with the diameter d. Assume that the roll is subjected to distributed load w=100N/mm and simply supported at both ends as shown in Figure 1. To design the hollow rolls as shown in Figure 1, attention should be paid to the maximum tensile stresses and stress amplitude appearing at the edges of the sleeve [13]. The friction coefficient among the sleeve, the spacer rings and the shafts is assumed as 0.3.

Table 1 shows the material properties of ceramics and steel. Stainless steel is usually used for rolls; however ceramic rolls may provide a longer maintenance span due to their high corrosion resistance and high abrasion resistance.

Figure 2 shows the finite element mesh model of the rolls. The total number of elements is 42920 and the total number of nodes is 53382. The model of 1/4 of the roll is considered due to symmetry.

2.2. Maximum Tensile Stress
The shrink fitting ratio when $\delta/d \leq 3.0 \times 10^{-4}$ will be considered because large values of δ/d are not suitable for ceramics. Figure 3 shows σ_θ under the shrink fitting ratio δ/d=3.0×10^{-4} and h=30mm. Figure 3 (a) shows the stress $\sigma_{\theta s}$ due to shrink fitting and Figure 3 (b) shows the stress $\sigma_{\theta max}$ ($=\sigma_{\theta s}+\sigma_{\theta b}$) due to load distribution w=100N/mm after shrink fitting. As shown in Figure 3 (a), the maximum tensile stress at point A and A' are 94.52MPa under the shrink fitting, which becomes 92.70MPa at point A by applying the distribution load after shrink fitting and becomes 93.88MPa at point A' as shown in Figure 3 (b). Maximum stress after applying the load distribution 96.60MPa appears at point B also shown in Figure 3 (b).

2.3. Effect of Shrink Fitting Ratio and Bending Moment upon the Maximum Tensile Stress $\sigma_{\theta max}$
Figure 4 (a) shows the relationship between $\sigma_{\theta s}$ and $\sigma_{\theta max}=\sigma_{\theta s}+\sigma_{\theta b}$ vs. δ/d when the load distribution w=100N/mm is applied after shrink fitting. When δ/d is small, the effect of stress concentration at the end of contact area is large and the effect decreases with increasing shrink fitting ratio. From Figure 4 (a) it is found that $\sigma_{\theta max}$ has a minimum value at about δ/d=1.0×10^{-4} when h=30mm. When, $\delta/d \geq 1.0 \times 10^{-4}$ $\sigma_{\theta max}$ increases linearly. In addition, $\sigma_{\theta s}$ increases linearly with increasing δ/d at h=30mm. On the other hand, $\sigma_{\theta b}$ decreases with increasing δ/d as shown in Figure 4 (b).
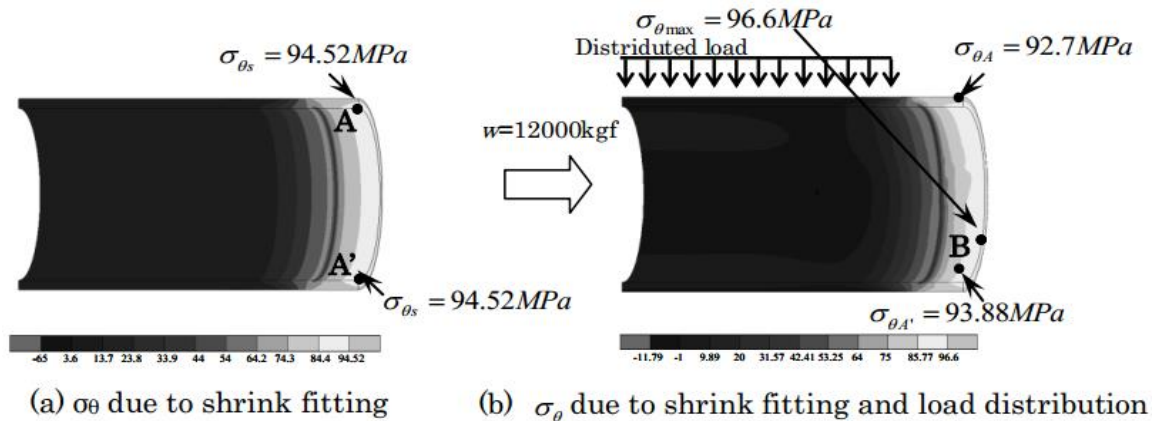
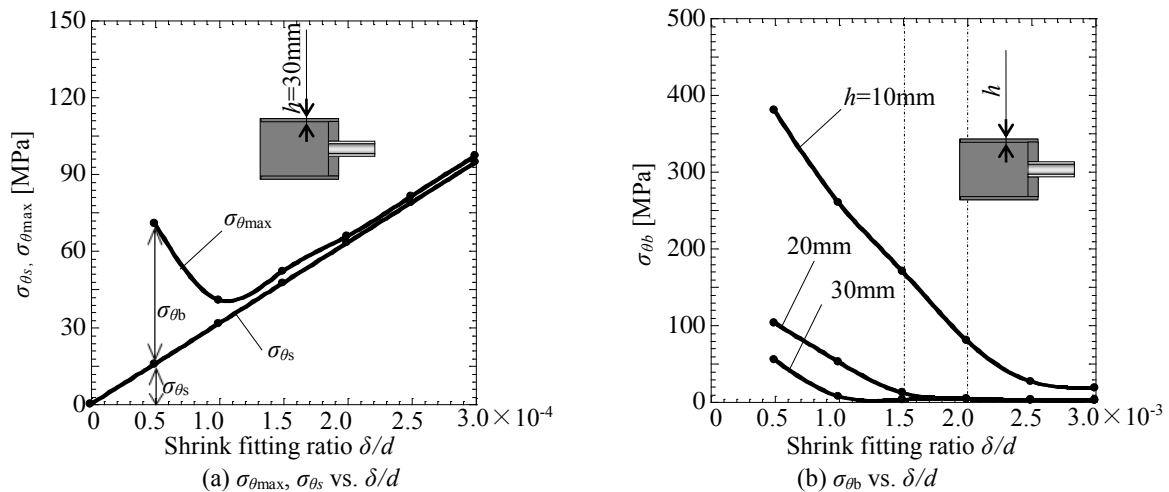**Figure 3** Stress distribution on the sleeve when $\delta/d = 3.0 \times 10^{-4}$

Figure 4 σ_θ vs. δ/d ($\sigma_{\theta max} = \sigma_{\theta s} + \sigma_{\theta b}$)

Here, Figure 4 (b) shows $\sigma_{\theta b} = \sigma_{\theta max} - \sigma_{\theta s}$ vs. δ/d relation for different sleeve thickness h. We assume the thickness as $h=10$mm, 20mm and 30mm. From Figure 4 (b), it is found that $\sigma_{\theta b}$ decreases with increasing sleeve thickness h. Also, when $h=20$mm and 30mm, $\sigma_{\theta b}$ becomes constant value over the threshold value of δ/d. That means, when the δ/d is large enough, the spacer rings and the sleeve can be treated as a unit body bonded perfectly [1].

2.4. Fatigue Strength Analysis

Fatigue strength should be also considered for ceramic rolls. Figure 5 shows the mean stress $\sigma_m = (\sigma_{\theta E} + \sigma_{\theta E'})/2$ and the stress amplitude $\sigma_a = (\sigma_{\theta E} - \sigma_{\theta E'})/2$. Due to the rotation of rolls, the values of stress σ_θ at the upper and the lower inside of sleeve are different as shown in Figure 5. Figure 6 shows an endurance limit diagram for $h=10$mm [14, 15]. In Figure 6, with increasing the shrink fitting ratio δ/d, the stress amplitude σ_a decreases. As shown in Figure 6, the values of stress amplitude σ_a and mean stress σ_m are below the fatigue strengths of ceramics for plain specimen when $\delta/d > 1.0 \times 10^{-4}$. In other words, the fatigue strength can be larger by using larger shrink fitting ratio.

2.5. Maximum Stress Appearing at the Outer Surface of Sleeve instead of Inner Surface of Sleeve

In Figure 7 (a) for $h=30$mm $\sigma_{\theta smax}$ appears at point A (shown in Figure 3 (a)) on the inner sleeve surface. However, in Figure 7 (b) for $h=10$mm $\sigma_{\theta smax}$ appears at the outer sleeve surface. Two-dimensional shrink fitting systems usually induce tensile stress for outer components and compressive stress for inner components. Then, the maximum tensile stress usually appears at the inner surface of outer components. To understand why the maximum stress appears at the outer surface, the stress
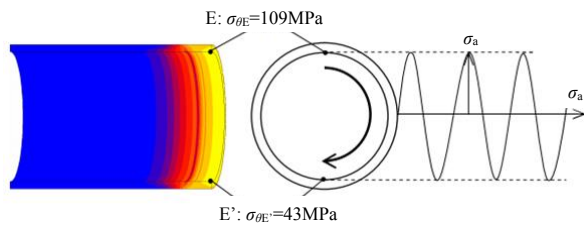
Figure 5 Cycle stress model
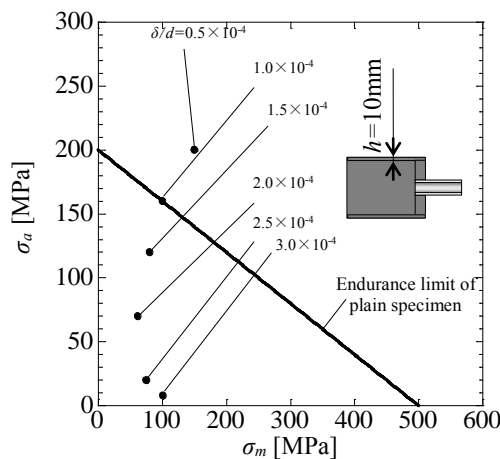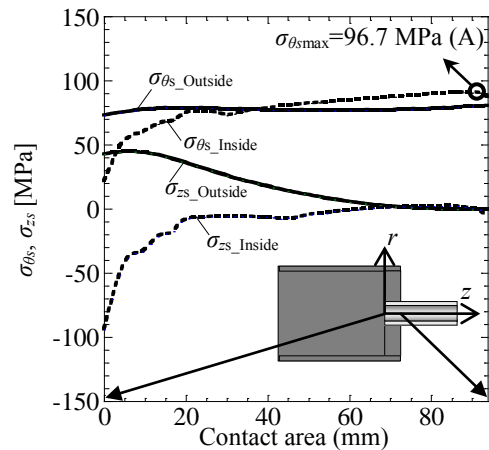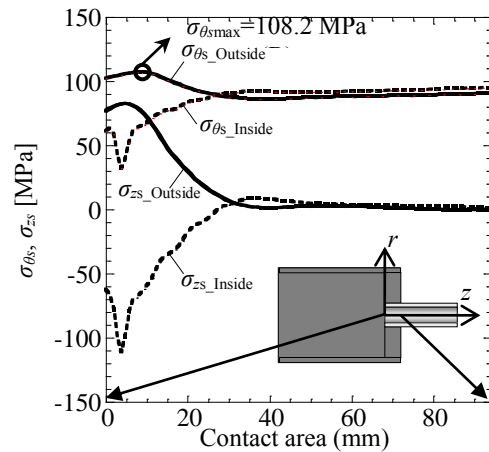(The value of stress when δ/d=3.0×10^{-4})

Figure 6 Endurance limit diagram for h=10mm

(a) σ_θ, σ_z vs. contact area for h=30mm

(b) σ_θ, σ_z vs. contact area for h=10mm

Figure 7 Shrink fitting stress distribution on
the sleeve when δ/d=3.0×10^{-4}

distributions are compared along the inner and the outer surfaces as shown in Figure 7. Figure 7 (a), (b) indicates that at the left contact end for both h=30mm and h=10mm the outer surface stress is larger than the inner one. It may be concluded that in they three-dimensional partial shrink fitting as shown in Figure 7 the outer stress is always larger than the inner stress. When h=30mm, since the inner stress at the right end is larger than the outer stress at the left end, the maximum stress is on the inner surface similar to 2D shrink fitting system. Care should be taken for the position of the maximum stress to design the ceramic sleeve roll different from the 2D system.

3. Heat-transfer coefficient Analysis

3.1. Analytical Conditions
Besides the ceramic roll, thermal stress should be consider for ceramic stokes dipped into molten metal, which have been used for low-pressure die casting [16]. Usually coefficient of thermal shock has been useful to measure often used to measure the severity [17]. In our previous studies, therefore, simple two-dimensional circular geometries were assumed and the heat transfer coefficients for ceramic structurers dipped into molten aluminum and molten zinc under unsteady flow were analyzed to discuss the thermal stress [3, 7, 18, 19]. Few studies targeting except molten aluminum and molten zinc are available for two-dimensional heat transfer coefficients [20-23]. In this study, two- and three-dimensional cylindrical geometries will be considered and compared with each other to analyze heat-

Table 2 Material properties of molten zinc and aluminum

Physical property	Zinc (420℃)	Aluminum (750℃)
Thermal conductivity, λ（W/m·K）	58.8	112
Kinematic viscosity, ν（mm^2/s）	0.489	0.96
Isobaric specific heat, C_p（kJ/kg·K）	0.505	1.10
Viscosity, η（mPa·s）	3.26	2.20
Prandtl number, P_r	0.028	0.022

Table 3 Material properties of ceramics

Mechanical property	Sialon
Thermal conductivity,（W/m·K）	17
Specific heat,（J/kg·K）	650
Coefficient of linear expansion,（1/K）	3.0×10^{-6}
Young's modulus,（GPa）	294
Specific weight	3.26
Poisson's ratio	0.27
4 Point bending strength,（MPa）	1050
Fracture toughness,（MN/mm$^{3/2}$）	7.5

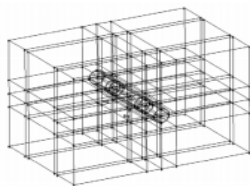

Figure 8 Mesh for 3D model
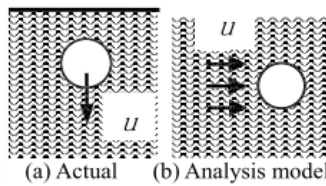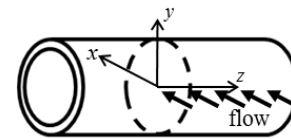

(a) Actual   (b) Analysis model

Figure 9 Modeling

Figure 10 rectangular coordinates

Table 4 Results of heat-transfer coefficient for different models in molten aluminium (α: W/m^2·K×10^3)
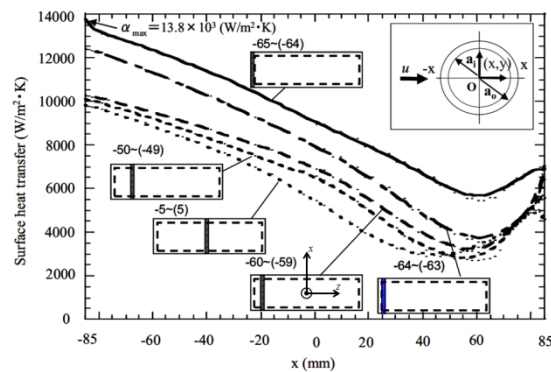

Figure 11 Heat-transfer coefficient as a function of x for cylindrical model in molten aluminum

transfer coefficient when ceramic structures is dipping into molten metal. Here, elliptical and rectangular shapes will be also considered in comparison with the cylindrical shape.

Three-dimensional mesh model shown in Figure 8 was generated by using commercial softwares SOLIDWORKS and GAMBIT2.4.6. The hexahedral mesh is used. The element number is about 3,000,000. Since the dipping of the circular body in Figure 9 (a) is equivalent to the flow problem around the circular body in Figure 9 (b), Figure 9 (b) will be considered. In present study, ANSYS Fluent 6.3.26(Fluent Inc.) was used for calculation with Navier-Stokes equations for a flow of an incompressible viscous fluid being solved using Finite Volume Method (FVM).

Table 2 shows material properties of molten zinc and aluminum. Table 3 shows material properties of ceramics.

To calculate the heat-transfer coefficient more accurately, the finite volume method is applied to the static 2D heat-transfer model. Here, the roll is fixed, and the fluid velocity is assumed as u= 25 mm/s. By using 3Dmodel, the effect of tiriteness the z-direction is also discussed.

3.2. Effects of 2D Models Shape on Heat-transfer coefficient
Table 4 shows the results of the heat-transfer coefficient when the flow rate u=25mm/s of molten aluminum for different ceramic geometries of 2D circle, 3D cylinder, 2D rectangle and 2D ellipse. In Table4, a is miner radius and b is major radius of ellipse. To compare with the rectangle $a : b$ is
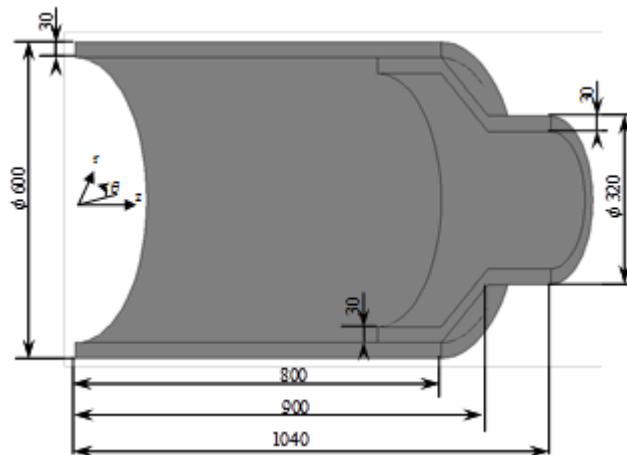
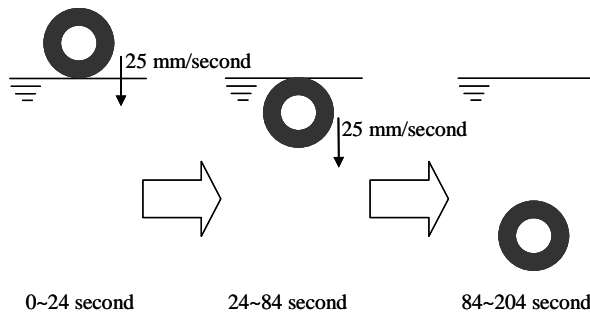**Figure 12** Dimensions of 1/4 cylindrical model (mm)

Table 5 Material properties of Si$_3$N$_4$

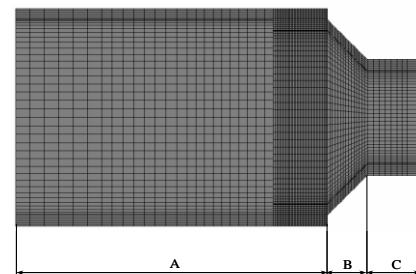|	
Thermal conductivity [W/m•K]	65
Specific heat [J/kg•K]	680
Thermal expansion coefficient [1/K]	3.0×10^{-6}
Young's modulus [GPa]	300
Tensile strength [MPa]	500
Mass density [kg/m^3]	3200
Poisson's ratio	0.3
Fracture toughness [MPa$\sqrt{}$ m]	7.7

Figure 13 Dipping process

Figure 14 FEM model of ceramics

assumed as 20 : 650. From Table 4, the maximum heat-transfer coefficient appears at the front end of 2D circle and 2D rectangle. With increasing a/b, the maximum heat-transfer coefficient increases.

3.3. Heat-transfer coefficient during Dipping in Horizontal Direction
Figure 11 shows the results of the heat-transfer coefficient of 3D cylinder. Each line shows the results for fixed value of the position z (see Figure 10). From Figure 11, it is found that the results of z=0 almost coincide with the 2D results. In Figure 11, the maximum heat-transfer coefficient α_{max}= 13.8×10^3(W/m^2 · K) and the minimum heat-transfer coefficient α_{min}=3.0×10^3(W/m^2 · K) . Therefore, the value of α_{max} is about 4 times larger than the value of α_{min}.

4. Thermal Stress Analysis of Ceramic Rolls Considering Separation

4.1. Analytical conditions
In this study, it is necessary to consider the thermal local deformations for the sleeve and the shaft in addition to the heat-transfer analysis for the whole structure shown in Figure12. The thermal-mechanical coupled analysis is therefore performed using three-dimensional hexahedral element with eight nodes. The dimensions are shown in Figure 12. In addition, the temperature of molten metal is 480°C and the initial temperature of roll is 20°C. The sleeve and the shaft are connected by shrink fitting. Define the shrink fitting ratio as δ/d, where δ is the diameter difference with the diameter d. Here, δ/d=2.0×10^{-4} is used for investigation. Here, silicon nitride (Si$_3$N$_4$) [24] having a high thermal conductivity is assumed for the analysis as shown in Table 5. Moreover, the dipping process is shown in Figure 13. The Roll is gradually dipped into molten metal at 25mm/s from 0s to 84s, while it reaches a steady state from 84s to 204s. Surface heat-transfer coefficient is calculated by FVM software ANSYS Fluent 6.3.26 for the roll dipped into the molten metal, which has a sleeve connected with two shafts by shrink fitting. In actual analysis, the roll is fixed and molten metal flows from the -
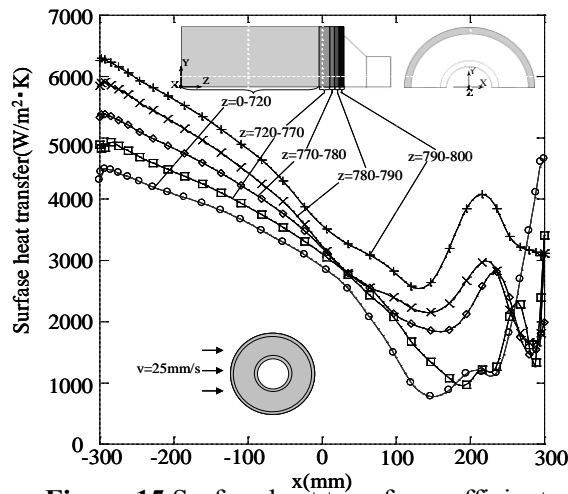
Figure 15 Surface heat transfer coefficient as a function of x for roll in the molten zinc
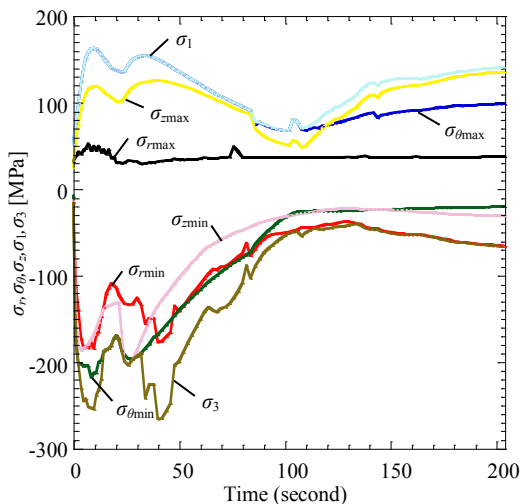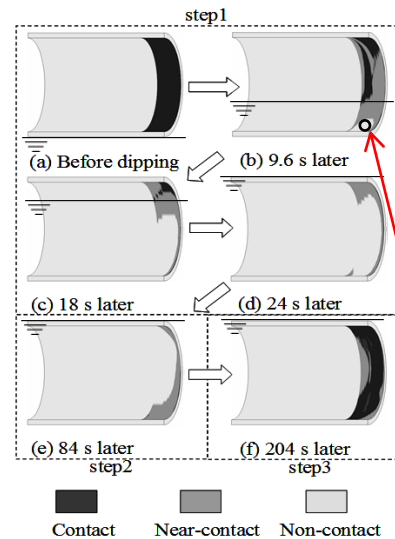

Figure 16 Contact status of the sleeve during dipping

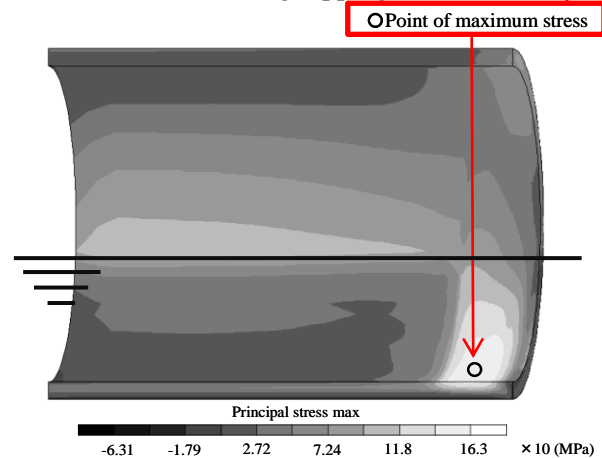**Figure 17** Maximum stress vs. time for sleeve

Figure 18 Stress distribution on the sleeve

x-direction to the x-direction at 25 mm/s. Figure 14 shows FEM model. The results of surface heat-transfer coefficients on part A (see Figure 14) of the roll are shown in Figure 15. The maximum of the surface heat-transfer coefficient is 6264 W/m^2・K at the position (x=-350mm and z= 800 mm) as shown in Figure 15. Here, as the heat-transfer coefficient at the internal surface of the roll α_{min}=1.0×10^3(w/m^2・K) is assumed, which is the minimum value of the outer surface. After when the roll is installed at the position of 2100mm in Figure 13 the same minimum heat-transfer coefficient α_{min}=1.0×10^3(w/m^2・K) is used. Thermal stress analysis is performed by FEM in the following.

4.2. Thermal Stress Considering Separation during Dipping

Figure 16 shows the contact status of ceramics roll shown in Figure 12 during dipping. It can be seen that the contact area becomes less during dipping. There is almost no contact at 24s after the roll is dipped into molten metal as shown in Figure 16 (d). However, as dipping goes on, the sleeve and the shaft become contacted again after 204s as shown in Figure 6 (f). Figure 17 shows the maximum and minimum stresses on the sleeve with time during dipping. Here, principal stress (σ_1: Maximum principal stress, σ_3: Minimum principal stress) and the stress components in cylindrical coordinate (σ_r, σ_θ, σ_z) are indicated. Maximum tensile stress σ_{1max}=162.7MPa appears on the sleeve at 9.6s after dipping as shown in Figure 17. The maximum tensile stress σ_{1max}=162.7MPa is smaller than the tensile strength of Si$_3$N$_4$ 500MPa (Safety factor=3.0). Figure 18 shows the stress distributions for the sleeve

when maximum tensile stress appears. It can be seen from Figure 18 that maximum tensile stress on the sleeve appears on the inside surface at the bottom end where is separated from the shaft (see Figure 16). The contact status of the sleeve with the shaft affects the thermal deformation of the sleeve. This is because heat conduction between the sleeve and the shaft is not performed if they are separated each other.

References
[1]   N.A. Noda, Hendra, Y. Takase, M. Tsuyunaru: Jounal of Solid Mechanics and Materials Engineering, 2(2008), 11, 1410-1419.
[2]   Hendra, M. Tsuyunaru, N.A. Noda, Y. Takase: *Key Engineering Materials*, 385-387(2008), 513-516.
[3]   W. Li, N.A. Noda, H. Sakai, Y. Higashi: *Key Engineering Materials*, 452-453(2011), 241-244.
[4]   W. Li, Ph.D dissertation, Kyushu Institude of Technology, 2012, 12
[5]   N.A. Noda, Y. Yamada, Y. Sano, S. Sugiyama, S. Kobayashi: *Engineering Failure Analysis*, 15(2008), 4, 261-274.
[6]   N.A. Noda, Hendra, Y. Takase, W. Li: *Jounal of Solid Mechanics and Materials Engineering*, 3(2009), 10, 1090-1100.
[7]   N.A. Noda, Hendra, Y. Takase, H. Ogura, Y. Higashi: *Jounal of Solid Mechanics and Materials Engineering*, 4(2010), 8, 1198-1213.
[8]   Y. Takase, W. Li, Hendra, H. Ogura, Y. Higashi, N.A. Noda: *Key Engineering Materials*, 452-453(2011), 233-236.
[9]   T. Iwata, H. Mori: *Plant Engineer*, 15(1983), 6, 55-59.
[10] N.A. Noda, Hendra, M. Oosato, K. Suzumoto, Y. Takase, W. Li: *Key Engineering Materials*, 462-463(2011), 1140-1145.
[11] N.A. Noda, Y. Sano, Y. Takase, W. Li, H. Sakai: *International Journal of Engineering Innovation and Management*, 1(2011), 77-82.
[12] S. Hamada, E. Ogawa, K. Shimizu, N.A. Noda, K. Kishi, S. Koga, sokeizai, 51, 12(2010), 54-58.
[13] S. Harada, N.A. Noda, O. Uehara, M. Nagano: *Transactions of the Japan Society of Mechanical Engineering* A, 57(1991), 539, 173-178.
[14] M. Masuda, T. Soma, M. Matsui, I. Oda: *Journal of the Ceramic Society of Japan*, 96(1988), 3, 277-283.
[15] M. Masuda, T. Makino. Y. Nakasuji, M. Matsui: *Materials Science & Technology*, (1993), 55-70.
[16] Y. Harada, K. Komatsu, N. Nomura, Patent Application Publication, No. H3-63565, 1991.
[17] JSME Data Book, Heat Transfer 5th Edition, 2009.
[18] N.A. Noda, M. Yamada, Y. Sano, S. Sugiyama, S. Kobayashi: *Transactions of the Japan Society of Mechanical Engineering* A, 70(2004), 700, 1755-1763.
[19] Hendra, PhD dissertaion, Kyusyu Instutude of Technology, 2010, 9
[20] H. Nakamura, K. Kamemoto: *Transactions of the Japan Society of Mechanical Engineering* B, 67(1996), 662, 2525-2532.
[21] K. Sugiyama, R. Ishiguro: *Transactions of the Japan Society of Mechanical Engineering* B, 51(1985), 464, 1269-1276.
[22] M. Shimizu, T. Nakagawa, Y. Kikuchi: *Transactions of the Japan Society of Mechanical Engineering*., 0.35-1(2003), 203-204.
[23] K. kawakita, N. Takenaka, D, Akie: *Transactions of the Japan Society of Mechanical Engineering*., 02-1(2002), 253-254.
[24] H. Imamura, M. Sohue, S. Hamayoshi, Patent Application Publication, No. H14-293642, 2002.
[25] N.A. Noda, D. Suryadi, S. Kumasaki, Y. Sano, Y. Takase: *Engineering Failure Analysis*, 57(2015), 261-274.
[26] N.A Noda, Y. Xu, D. Suryadi, Y. Sano, Y. Takase: *Journal of ISIJ International*, 56(2016), 2, 303-310.